

Relativistic multireference many-body perturbation theory calculations on F-, Ne-, Na-, Mg-, Al-, Si- and P-like xenon ions

Marius J Vilkas¹, Yasuyuki Ishikawa¹ and Elmar Träbert^{2,3}

¹ Department of Chemistry, University of Puerto Rico, PO Box 23346 San Juan, Puerto Rico 00931-3346, USA

² Experimentalphysik III, Ruhr-Universität Bochum, D-44780 Bochum, Germany

³ High Temperature and Astrophysics Division, LLNL, PO Box 808, Livermore, CA 94550, USA

E-mail: traebert@ep3.rub.de

Received 20 January 2006, in final form 29 March 2006

Published 24 April 2006

Online at stacks.iop.org/JPhysB/39/2195

Abstract

Many-body perturbation theory (MBPT) has been employed to calculate with high wavelength accuracy the extreme ultraviolet (EUV) spectra of F-like to P-like Xe ions. We discuss the reliability of the new calculations using the example of EUV beam–foil spectra of Xe, in which $n = 3$, $\Delta n = 0$ transitions of Na-, Mg-, Al- and Si-like ions have been found to dominate. A further comparison is made with spectra from an electron beam ion trap, that is, from a device with a very different (low density) excitation balance.

1. Introduction

Regular surveys of the data holdings of, for example, the NIST atomic spectra data base [1] show how only for elements up to about $Z = 26$ (Fe) there are at least some data for practically all charge states (though often deplorably incomplete). For heavier elements, data are mostly limited to neutral atoms and the first few ionization stages, calculated values for one- and two-electron ions, and resonance lines of ions with a single valence electron (Na-like, Cu-like). The general character of spectra of any ion species can nowadays be quickly derived from calculations. However, most of these calculations fall far short of spectroscopic accuracy. If an experimental spectrum was to show a few hundred lines, and the theory predicted a few hundred lines, there would be no easy mapping of one set to the other, and most likely it would turn out (as it regularly does) that the experiment shows a plenitude of lines that are not identifiable from current calculations. As an example, we cite the long-drawn and not yet fully successful quest for the analysis of beam–foil spectra of four- to six-electron ions of an element as light as Ne ($Z = 10$) [2–6]. It would be a mark of substantial progress if even the

most prominent lines in spectra of ions with two to four valence electrons could be predicted well enough to enable immediate identification within the experimental and calculational uncertainties.

Of course, most calculations can be adjusted to some experimental atomic structure parameters, and such scaled calculations can then predict further atomic data with improved reliability. A test that precludes such a bias would require uncharted experimental data and unadjusted, that is, *ab initio* calculations. We resort to experimental data for atomic systems well beyond the bulk of well-analysed spectra, and thus with some uncertainty in the earlier line classifications. The data are from a series of beam-foil experiments on Xe and Au [7–9] that have, about a decade ago, pushed the envelope of such enterprises. (One of us, ET, was the lead author of those three studies, and some of the laboratory notes and other unpublished materials of the time are available to us for a re-investigation.) In the present paper, we concentrate on the Xe data which are not as far beyond well-charted territory as are the Au data (which will be discussed elsewhere). We also compare our results to Xe spectra recently obtained at the Livermore electron beam ion trap SuperEBIT [10], that is, a light source with very different excitation conditions; those spectra also are of much higher spectral resolution than the earlier beam-foil spectra. There is very little other experimental information on the EUV spectra of such highly charged Xe ions as we discuss, and most of that [11–13] is on $n = 2-3$ transitions in Ne-like ions which we do not cover. Xe has recently found interest in the context of developing a light source for EUV lithography; the charge states needed to produce light at a wavelength near 135 Å are much lower though than the ones discussed here (about $q = 8+$ versus $q = 39+$ to $q = 45+$). Intermediate to these two ranges of charge states are investigations of EUV light emission from a low-inductance vacuum spark [14], emission spectra after electron capture by Xe ions of $q = 8+$ to $16+$ from He gas [15], and studies at the Berlin EBIT [16] of EUV spectra of Xe¹⁷⁺ to Xe²⁵⁺.

The EUV spectra of highly charged multi-valence-electron ions, such as Mg-like to P-like Xe ions, comprise a large number of emission lines, typically several thousand, and the highly accurate relativistic many-body theory must be brought to bear on the electronic structure of low- to high-lying excited levels of the complex ions. Relativistic, electron correlation and quantum electrodynamic (QED) effects play important or even dominant roles and must be accurately accounted for when trying to interpret the complex EUV spectra.

In recent years, relativistic many-body methods have evolved to the point where they can predict the term energies and decay probabilities of one-valence-electron ions with unprecedented accuracy [17–20]. However, high-accuracy theoretical predictions for multivalence-electron ions of a quality comparable to those for one-valence-electron ions have been unsuccessful for some years. The major difficulty in developing a high-accuracy many-body algorithm for multivalence-electron systems lies in near-degeneracy in the valence shells and accurate description of valence-core dynamic correlation. We have recently developed and implemented such a relativistic multi-reference Møller-Plesset (MR-MP) perturbation theory for high-accuracy calculations of spectroscopic quality for the term energies and decay probabilities of multivalence-electron ions [21, 22].

We apply our multi-reference Møller-Plesset calculations to determine levels and transition probabilities in F- to P-like ions of Xe and to obtain theoretical predictions of a multitude of prominent transitions in the spectral range of the observations. We simulate spectra for a visual comparison with the available data. It turns out that such calculations alleviate the calibration problem in the beam-foil data, largely explain even minor features in the observed spectra and appear to be eminently useful guides for future experiments.

2. Theory

The effective N -electron Hamiltonian (in atomic units) for the development of our relativistic MR–MP algorithm is taken to be the relativistic ‘no-pair’ Dirac–Coulomb–Breit (DCB) Hamiltonian [23, 24]

$$H_{\text{DCB}}^+ = \sum_i h_D(i) + \mathcal{L}_+ \left(\sum_{i>j} \frac{1}{r_{ij}} + B_{ij}(0) \right) \mathcal{L}_+ \quad (1)$$

with

$$B_{ij}(0) = -\frac{1}{2} [\alpha_i \cdot \alpha_j + (\alpha_i \cdot \mathbf{r}_{ij})(\alpha_j \cdot \mathbf{r}_{ij})/r_{ij}^2] / r_{ij}. \quad (2)$$

Here $h_D(i)$ is the Dirac one-electron Hamiltonian. The DCB Hamiltonian is covariant to first order and increases the accuracy of calculated fine-structure splittings and inner-shell binding energies. Higher order QED effects appear first in order α^3 . The nucleus was simulated as a sphere of uniform proton charge with the radius $R = A^{1/3}$, where A is the atomic mass. $\mathcal{L}_+ = L_+(1)L_+(2) \cdots L_+(N)$, where $L_+(i)$ is the projection operator onto the space $D^{(+)}$ spanned by the positive-energy eigenfunctions of the matrix Dirac–Fock–Breit (DFB) SCF equation [24]. \mathcal{L}_+ is the projection operator onto the positive-energy space $\mathfrak{D}^{(+)}$ spanned by the N -electron configuration-state functions (CSF) constructed from the positive-energy eigenfunctions of the matrix DFB SCF. It takes into account the field-theoretic condition that the negative-energy states are filled. The eigenfunctions $\{\phi_{n_q\kappa_q}^{(\pm)}(r)\} (\in D^{(+)} \cup D^{(-)})$ of the matrix DFB SCF equation clearly separate into two discrete manifolds, $D^{(+)}$ and $D^{(-)}$, respectively, of positive- and negative-energy one-particle states. As a result, the positive-energy projection operators can be accommodated easily in many-body calculations. The formal conditions on the projection are automatically satisfied when only the positive-energy spinors are employed.

N -electron eigenfunctions of the no-pair DCB Hamiltonian are approximated by a linear combination of M_{MC} configuration-state functions, $\{\Phi_I^{(+)}(\gamma_I \mathcal{J} \pi); I = 1, 2, \dots, M_{\text{MC}}\} \in \mathfrak{P}^{(+)}$, constructed from positive-energy eigenfunctions of the matrix multiconfiguration Dirac–Fock–Breit (MCDFB) SCF equation,

$$\psi_K^{\text{MC}}(\gamma_K \mathcal{J} \pi) = \sum_I^{M_{\text{MC}}} C_{IK} \Phi_I^{(+)}(\gamma_I \mathcal{J} \pi). \quad (3)$$

The MCDFB SCF wavefunction $\psi_K^{\text{MC}}(\gamma_K \mathcal{J} \pi)$ is an eigenfunction of the angular momentum and parity operators with total angular momentum \mathcal{J} and parity π . γ denotes a set of quantum numbers other than \mathcal{J} and π necessary to specify the state uniquely.

Second-order variation of the state-averaged energy $\Omega_{\text{state-ave}}$ [21] is taken with respect to the matrix elements of spinor unitary rotation matrix and configuration mixing coefficients $\{C_{IK}\}$, leading to the Newton–Raphson equations for second-order MCDFB SCF [25]. This state-averaged second-order MCDFB equation yields a single set of spinors for the ground and low-lying even- and odd-parity excited $(\gamma, \mathcal{J}, \pi)$ levels.

In order to account for strong configuration mixing among the highly excited levels, the multireference configuration interaction method (MR–CI) [26] is introduced in an extended subspace $\mathfrak{P}_{\text{CI}}^{(+)}$ of positive-energy space. N -electron eigenfunctions of the no-pair DCB Hamiltonian are approximated by a linear combination of $M_{\text{CI}} (\gg M_{\text{MC}})$ configuration-state functions, $\{\Phi_I^{(+)}(\gamma_I \mathcal{J} \pi); I = 1, 2, \dots, M_{\text{CI}}\}$, constructed from the one-particle positive-energy spinors computed in matrix MCDFB SCF. Variation of the configuration-state coefficients $\{C_{IK}\}$ leads to the determinantal CI equation.

$$\det \left(\langle \Phi_I^{(+)}(\gamma_I \mathcal{J} \pi) | H_{\text{DCB}}^+ | \Phi_J^{(+)}(\gamma_J \mathcal{J} \pi) \rangle - E^{\text{CI}} \langle \Phi_I^{(+)}(\gamma_I \mathcal{J} \pi) | \Phi_J^{(+)}(\gamma_J \mathcal{J} \pi) \rangle \right) = 0. \quad (4)$$

The eigenfunctions $\{\psi_K^{\text{CI}}(\gamma_K \mathcal{J}\pi)\}$ form a subspace $\mathfrak{P}_{\text{CI}}^{(+)}$ of the positive-energy space $\mathfrak{D}^{(+)}$.

$$\psi_K^{\text{CI}}(\gamma_K \mathcal{J}\pi) = \sum_I^{M_{\text{CI}}} C_{IK} \Phi_I^{(+)}(\gamma_I \mathcal{J}\pi), \quad K = 1, 2, \dots, M_{\text{CI}}. \quad (5)$$

The total DCB energy of the general CI state $|\psi_K^{\text{CI}}(\gamma_K \mathcal{J}\pi)\rangle$ can be expressed as

$$\begin{aligned} E_K^{\text{CI}}(\gamma_K \mathcal{J}\pi) &= \langle \psi_K^{\text{CI}}(\gamma_K \mathcal{J}\pi) | H_{\text{DCB}}^+ | \psi_K^{\text{CI}}(\gamma_K \mathcal{J}\pi) \rangle \\ &= \sum_{I,J=1}^{\mathfrak{P}_{\text{CI}}^{(+)}} C_{IK} C_{JK} \langle \Phi_I^{(+)}(\gamma_I \mathcal{J}\pi) | H_{\text{DCB}}^+ | \Phi_J^{(+)}(\gamma_J \mathcal{J}\pi) \rangle. \end{aligned} \quad (6)$$

Here it is assumed that $\psi_K^{\text{CI}}(\gamma_K \mathcal{J}\pi)$ and $\Phi_I^{(+)}(\gamma_I \mathcal{J}\pi)$ are normalized.

The frequency-dependent Breit interaction, normal mass shift (NMS) and specific mass shift (SMS) are evaluated as the first-order corrections using the eigenvectors $\{\psi_K^{\text{CI}}(\gamma_K \mathcal{J}\pi)\}$ from the MR-CI [21]. The frequency dependence of the Breit interaction is evaluated in the Coulomb gauge, subtracting frequency-independent Breit interaction which is already included ($B^{(0+)}(0)$) in MR-CI (equation (6)). The first-order corrections calculated in this way are denoted by $\Delta B^{(1)}(\omega)$.

The no-pair DCB Hamiltonian H_{DCB}^+ is decomposed into two parts, unperturbed Hamiltonian H_0 and perturbation V , following Møller and Plesset [27],

$$H_{\text{DCB}}^+ = H_0 + V, \quad (7)$$

$$H_0 = \sum_I^{\mathfrak{D}^{(+)}} |\Phi_I^{(+)}(\gamma_I \mathcal{J}\pi)\rangle E_I^{\text{CSF}} \langle \Phi_I^{(+)}(\gamma_I \mathcal{J}\pi)|, \quad (8)$$

so that

$$H_0 |\Phi_I^{(+)}(\gamma_I \mathcal{J}\pi)\rangle = E_I^{\text{CSF}} |\Phi_I^{(+)}(\gamma_I \mathcal{J}\pi)\rangle (I = 1, 2, \dots). \quad (9)$$

E_I^{CSF} is a sum of the products of one-electron energies defined by ε_q^+ and an occupation number $n_{n_q \kappa_q}[I]$ of the κ_q -symmetry shell in the CSF $\Phi_I^{(+)}(\gamma_I \mathcal{J}\pi)$ [28, 29];

$$E_I^{\text{CSF}} = \sum_q^{D^{(+)}} \varepsilon_q^+ n_{n_q \kappa_q}[I]. \quad (10)$$

The subset, $\{\Phi_I^{(+)}(\gamma_I \mathcal{J}\pi); I = 1, 2, \dots, M_{\text{CI}}\}$, with which we expand the CI wavefunction $\psi_K^{\text{CI}}(\gamma_K \mathcal{J}\pi)$ (equation (5)) defines an active subspace $\mathfrak{P}_{\text{CI}}^{(+)}$ spanned by $\psi_K^{\text{CI}}(\gamma_K \mathcal{J}\pi)$ and its $M_{\text{CI}} - 1$ orthogonal complements, $\{\psi_K(\gamma_K \mathcal{J}\pi); K = 1, 2, \dots, M_{\text{CI}}\}$. The matrix of H_{DCB}^+ in this subspace is diagonal

$$\langle \psi_K^{\text{CI}}(\gamma_K \mathcal{J}\pi) | H_{\text{DCB}}^+ | \psi_L^{\text{CI}}(\gamma_L \mathcal{J}\pi) \rangle = \delta_{KL} (E_K^{(0)} + E_K^{(1)}) \quad \delta_{KL} E_K^{\text{CI}}(\gamma_K \mathcal{J}\pi), \quad (11)$$

where

$$E_K^{(0)} = \langle \psi_K^{\text{CI}}(\gamma_K \mathcal{J}\pi) | H_0 | \psi_K^{\text{CI}}(\gamma_K \mathcal{J}\pi) \rangle = \sum_I^M C_{IK} C_{IK} E_I^{\text{CSF}} \quad (12)$$

and

$$E_K^{(1)} = \langle \psi_K^{\text{CI}}(\gamma_K \mathcal{J}\pi) | V | \psi_K^{\text{CI}}(\gamma_K \mathcal{J}\pi) \rangle. \quad (13)$$

The residual space in the positive-energy subspace is $\mathfrak{Q}^{(+)} = \mathfrak{D}^{(+)} - \mathfrak{P}_{\text{CI}}^{(+)}$, which is spanned by CSFs $\{\Phi_I^{(+)}(\gamma_I \mathcal{J}\pi); I = M_{\text{CI}} + 1, M_{\text{CI}} + 2, \dots\}$.

Application of the Rayleigh–Schrödinger perturbation theory provides order-by-order expressions of the perturbation series for the state approximated by $|\psi_K^{\text{CI}}(\gamma_K \mathcal{J}\pi)\rangle$,

$$E_K(\gamma_K \mathcal{J}\pi) = E_K^{\text{CI}}(\gamma_K \mathcal{J}\pi) + E_K^{(2)} + \dots, \quad (14)$$

where

$$E_K^{(2)} = \langle \psi_K^{\text{CI}}(\gamma_K \mathcal{J}\pi) | V \mathcal{R} V | \psi_K^{\text{CI}}(\gamma_K \mathcal{J}\pi) \rangle. \quad (15)$$

Here, \mathcal{R} is the resolvent operator,

$$\mathcal{R} = \frac{\mathcal{Q}^{(+)}}{E_K^{\text{CSF}} - H_0} \quad (16)$$

with

$$\mathcal{Q}^{(+)} = \sum_I^{\Omega^{(+)}} |\Phi_I^{(+)}(\gamma_I \mathcal{J}\pi)\rangle \langle \Phi_I^{(+)}(\gamma_I \mathcal{J}\pi)|. \quad (17)$$

The projection operator $\mathcal{Q}^{(+)}$ projects onto the subspace $\Omega^{(+)}$ spanned by CSFs $\{\Phi_I^{(+)}(\gamma_I \mathcal{J}\pi); I = M_{\text{CI}} + 1, M_{\text{CI}} + 2, \dots\}$. Using the spectral resolution of the resolvent operator acting on $V|\Phi_I^{(+)}(\gamma_I \mathcal{J}\pi)\rangle$, the second-order correction may be expressed as

$$\begin{aligned} E_K^{(2)} &= \sum_{IJ} C_{IK} C_{JK} \langle \Phi_I^{(+)}(\gamma_I \mathcal{J}\pi) | V \mathcal{R} V | \Phi_J^{(+)}(\gamma_J \mathcal{J}\pi) \rangle \\ &= \sum_{L=M+1}^{\Omega^{(+)}} \sum_{I,J=1}^{\mathfrak{P}_{\text{CI}}^{(+)}} C_{IK} C_{JK} \frac{\langle \Phi_I^{(+)}(\gamma_I \mathcal{J}\pi) | V | \Phi_L^{(+)}(\gamma_L \mathcal{J}\pi) \rangle}{E_J^{\text{CSF}} - E_L^{\text{CSF}}} \\ &\quad \times \langle \Phi_L^{(+)}(\gamma_L \mathcal{J}\pi) | V | \Phi_J^{(+)}(\gamma_J \mathcal{J}\pi) \rangle. \end{aligned} \quad (18)$$

In this form, all perturbation corrections beyond first order describe residual dynamic correlation correction for the state approximated by the CI wavefunction $|\psi_K^{\text{CI}}(\gamma_K \mathcal{J}\pi)\rangle$.

Summations over the CSFs in equations (16) and (18) are restricted to CSFs ($\in \mathfrak{D}^{(+)}$) constructed from the positive-energy branch ($D^{(+)}$) of the spinors, effectively incorporating into the computational scheme the ‘no-pair’ projection operator \mathcal{L}_+ contained in the DCB Hamiltonians.

The large and small radial components of the Dirac spinors are expanded in sets of even-tempered Gaussian-type functions (GTF) that satisfy the boundary conditions associated with the finite nucleus [30]. The speed of light is taken to be 137.035 9895 au throughout this study. The GTFs that satisfy the boundary conditions associated with the finite nucleus are automatically kinetically balanced [30]. Even-tempered basis sets of 26s24p20d18f G spinors (G for ‘Gaussian’) for up to angular momentum $L = 3$ and 15 G spinors for $L = 4$ –11 are employed. The order of the partial-wave expansion L_{max} , the highest angular momentum of the spinors included in the virtual space, is $L_{\text{max}} = 11$ throughout this study.

All electrons have been included in the MR–MP perturbation theory calculations to determine accurately the effects of relativity on electron correlation. Radiative corrections (Lamb shifts) were estimated for each state by evaluating the electron self-energy and vacuum polarization following an approximation scheme discussed by Indelicato, Gorceix, and Desclaux [31]. The code described in [31, 32] was adapted to our basis set expansion calculations for this purpose: all the necessary radial integrals were evaluated analytically. In this scheme [32], the screening of the self-energy is estimated by integrating the charge density of a spinor to a short distance from the origin, typically 0.3 Compton wavelength. The ratio of the integral computed with an MCDFB SCF spinor and that obtained from the corresponding hydrogenic spinor is used to scale the self-energy correction for a bare nuclear charge that has

been computed by Mohr [33]. The QED corrections are substantial; the Lamb shift is of the order $10\,000\text{ cm}^{-1}$ for the ions of our sample.

The levels that we present have been calculated with extensive sets of MBPT wavefunctions. The transition rates have mostly been obtained by less time-consuming MCDF calculations. In most cases the results of Babushkin (length) gauge and Coulomb (velocity) gauge calculations agree with each other to within one to ten per cent. We present our level lifetime results with three significant figures. However, in some test cases (especially for several very low transition probabilities), MBPT lifetimes differ by up to 10% from the MCDF Babushkin gauge results. The calculated lifetimes therefore are considered reasonably good approximations, but could be improved upon in some cases by much more extensive calculations.

3. Experimental data

The experimental set-up of the beam-foil work on Xe and Au at the Darmstadt (Germany) GSI UNILAC accelerator has been described elsewhere [7–9]. This experimental arrangement has gone through various development stages; most of the experimental effort was directed at the precision spectroscopy of few-electron ions, in particular the determination of QED contributions to the transition energies of $n = 2\text{--}2$ transitions in Li- and Be-like ions [34–38]. In contrast, the spectral lines of interest in the present study are largely in a spectral range beyond the reach of calibration lines from the stationary calibration light source available. This shortage of external wavelength references necessitated the use of calculated internal ('in-beam') calibration lines, combined with a calculated dispersion curve.

The Xe experiment [7, 8] aimed primarily at spectra from which decay curves of the resonance lines of Na-like Xe ions were to be constructed and then atomic level lifetimes and transition probabilities derived. The wavelengths of the $3s\text{--}3p\text{--}3d$ transitions in Na-like ions can be calculated well enough for such purpose. The emission spectrum of the foil-excited ion beam was observed with a multichannel (spatially extended) detector that may record several spectral lines in parallel. The wavelength calibration of the grazing incidence spectrometer at GSI (with a $R = 5\text{ m}$ radius of curvature grating/5 m diameter Rowland circle), was established with the aid of a Penning discharge with Ne [39], Mg or Al that provided lines of wavelengths above about 130 Å . Careful angle measurements of the spectrometer ascertained that it viewed the ion beam at right angles, so that the observed spectral lines ought not to be shifted by the first order Doppler effect, while the correction for the second order (time dilation) was taken from the separately measured beam energy (ion velocity 11.2% of the speed of light, time dilation factor $\gamma = 1.0063$). However, the wavelength determination effort was very limited, because the lamp produced lines only near the upper wavelength end of the EUV observations.

The type of multichannel detector used is known to be rather linear in position information in the central part, but less so towards the edges. If precise wavelength measurements are being tried with such a detector, widely overlapping, well-calibrated spectra are a necessity. Such an approach was not compatible with the time frame of the given experiment.

The dispersion established in the wavelength range near $130\text{--}160\text{ Å}$ was used as an approximation throughout, relying on perceived line identifications of $n = 3\text{--}3$ transitions in Na-like ions for reference markers in the individual spectral sections. However, a constant dispersion was a reasonable approximation for only two of the three spectral slices, but not for the third. At short wavelengths, the dispersion (wavelength interval divided by distance along the Rowland circle circumference) progressively changes, and it should not have been taken as constant in [8]. Taking the spectrometer geometry into better account (now for all spectral

sections covered), changes the dispersion notably, so that—with reference to the same line of Na-like Xe in the short-wavelength spectrum—the probable identifications of several other lines change. The consequences are described below.

At the time of the Xe measurements (in 1993), the spectrometer had not yet reached its later higher resolving power. In principle, the spectra could be remeasured nowadays with a somewhat better resolution while using the same basic instrument, or with a flat-field spectrograph and a CCD camera, as employed at the Livermore electron beam ion traps [10]. Measurements at other ion beam energies could be used to enhance other charge states. However, the beam-foil measurement set-up at GSI has since been discarded. The same spectral range and charge states can be reached in laser-produced plasmas [40–42] and in electron beam ion traps [10]. Both of these techniques have different conditions (high versus low density) and therefore the spectra often look rather different. The beam-foil data are peculiar in the sense that the excitation takes place at very high density, whereas the observation is of ions in a low density environment, and it is intrinsically time-resolved on the scale of a few picoseconds.

At the given energy of 5.9 MeV amu^{-1} , the expected charge state distribution [43] of the foil-excited Xe ion beam was $q = 47+$ (N-like ions) 2%, $46+$ (O-like) 6%, $45+$ (F-like) 14%, $44+$ (Ne-like) 20%, $43+$ (Na-like) 22.5%, $42+$ (Mg-like) 18%, $41+$ (Al-like) 11%, $40+$ (Si-like) 4.5% and $39+$ (P-like) 1.2%. (Other calculations and tabulations differ by up to one charge state for the mean or the most abundant charge state.) Consequently, when using a sufficiently thick exciter foil (of a few hundred $\mu\text{g cm}^{-2}$ areal density, which is still absolutely thin), transitions between low-lying levels of these ions were expected to show in about the same pattern of overall intensities as the charge state distribution. This means about equal prominence of lines from Ne to Mg-like Xe ions, F- and Al-like ions at half this amount, and everything else being much weaker. Indeed, the strongest line was identified at the time (to be corrected below) with a transition in Ne-like Xe, and the weakest lines for which a classification was suggested were associated tentatively with Si-like Xe ions.

4. Comparison of calculational results with observations

According to the expected range of charge states expected in the spectra (see above), MR–MP term energies and lifetimes of excited levels were evaluated for each of these ions. The term energies and lifetimes of three representative ions, Ne-, Al- and Si-like Xe are displayed in tables 1 and 2. For these multivalence-electron ions, very few experimental and theoretical studies are available, whereas for Na- and Mg-like ions a literature search shows many more entries.

In table 1, theoretical excitation energies (term values) of the lowest 36 excited states of Ne-like Xe ion arising from the $2l^{-1} 3l'$ ($l = 0-1$, $l' = 0-3$) configurations are compared with available experimental data [44]. The energies were computed by subtracting the total energy of the ground $1s^2 2s^2 2p^6 {}^1S_0$ state from those of the excited levels. The term energies of 12 excited levels in the Ne-like ion have been evaluated by MBPT [45]; these are also given for comparison. For all the experimentally determined level energies, our MR–MP energies agree well with experiment, a majority of them to within the experimental error.

A fair number of other calculations and semiempirical analyses are available for ions along various isoelectronic sequences. These are, for example, for the Ne sequence [45–47], for Na-like ions [17, 18, 48, 50], for the Mg sequence [19, 51–57], for Al-like ions [20, 58, 59] and for the Si sequence [60–65]. With the exception of the Na sequence, in which experimental tests up to U^{81+} [66] have confirmed the high accuracy of the latest calculations, most isoelectronic sequence calculations are not extremely accurate—aiming for

Table 1. Comparison of the MR–MP calculated excitation energies E (eV) and lifetimes τ with experimental and other theoretical results in Ne-like xenon ion.

Level	J	E (MR–MP)	τ (ps)	E (Expt) ^a	E (MCDF) ^a	E (MBPT) ^b
$2s^2 2p^6$	0	0		0	0	0
$2p_{3/2}^{-1}3s_{1/2}$	2	4210.02		4210.2(2)	4208.88	4209.9
$2p_{3/2}^{-1}3s_{1/2}$	1	4215.48	0.030	4215.2(2)	4214.44	4215.21
$2p_{3/2}^{-1}3p_{1/2}$	1	4302.56	55.8			
$2p_{3/2}^{-1}3p_{1/2}$	2	4304.97	54.4	4305.3(2)	4304.29	4304.8
$2p_{3/2}^{-1}3p_{3/2}$	3	4390.41	7.07			
$2p_{3/2}^{-1}3p_{3/2}$	1	4390.42	7.85			
$2p_{3/2}^{-1}3p_{3/2}$	2	4398.68	6.36	4398.8(3)	4397.93	4398.5
$2p_{3/2}^{-1}3p_{3/2}$	0	4433.07	3.76			
$2p_{3/2}^{-1}3d_{3/2}$	0	4497.26	7.80			
$2p_{3/2}^{-1}3d_{3/2}$	1	4503.08	0.59			4502.47
$2p_{3/2}^{-1}3d_{3/2}$	3	4506.55	7.08			
$2p_{3/2}^{-1}3d_{3/2}$	2	4510.75	6.72			
$2p_{3/2}^{-1}3d_{5/2}$	4	4523.26	0.97			
$2p_{3/2}^{-1}3d_{5/2}$	2	4527.39	19.4			
$2p_{3/2}^{-1}3d_{5/2}$	3	4534.26	18.7			
$2p_{1/2}^{-1}3s_{1/2}$	1	4543.69	0.006	4543.5(2)	4542.42	4543.51
$2p_{1/2}^{-1}3s_{1/2}$	0	4544.26	113			
$2p_{3/2}^{-1}3d_{5/2}$	1	4557.76	0.002	4557.8(2)	4557.75	4557.96
$2p_{1/2}^{-1}3p_{1/2}$	1	4636.26	55.6			
$2p_{1/2}^{-1}3p_{1/2}$	0	4666.87	11.1			
$2p_{1/2}^{-1}3p_{3/2}$	1	4725.09	6.40			
$2p_{1/2}^{-1}3p_{3/2}$	2	4727.89	6.93	4728.4(5)	4726.92	4727.7
$2p_{1/2}^{-1}3d_{3/2}$	2	4839.77	6.95			
$2s_{1/2}^{-1}3s_{1/2}$	1	4854.37	0.466			
$2p_{1/2}^{-1}3d_{3/2}$	1	4856.89	0.002	4857.4(2)	4856.20	4856.78
$2p_{1/2}^{-1}3d_{5/2}$	2	4860.69	18.2			
$2p_{1/2}^{-1}3d_{5/2}$	3	4863.39	19.6			
$2s_{1/2}^{-1}3s_{1/2}$	0	4872.40	0.565			
$2s_{1/2}^{-1}3p_{1/2}$	0	4947.12	0.496			
$2s_{1/2}^{-1}3p_{1/2}$	1	4949.10	0.024	4949.2(4)	4951.60	4948.7
$2s_{1/2}^{-1}3p_{3/2}$	2	5035.54	0.466			
$2s_{1/2}^{-1}3p_{3/2}$	1	5039.68	0.010	5039.9(2)	5042.03	5039.3
$2s_{1/2}^{-1}3d_{3/2}$	1	5146.70	0.523			
$2s_{1/2}^{-1}3d_{3/2}$	2	5149.98	0.491			
$2s_{1/2}^{-1}3d_{5/2}$	3	5166.71	0.510			
$2s_{1/2}^{-1}3d_{5/2}$	2	5178.39	0.523	5178.8(2)	5181.22	5178.1

^a [44].^b [77].

accuracy usually puts high demands on computing power. This is in a way orthogonal to the approach chosen here, the calculation of accurate values for many ions of a given elemental species. Because of the different intentions, we refrain from direct comparisons with the results of other calculations, with the exception of a few examples for which experimental data are available as well (see below).

Table 2. MR–MP calculated term values E (cm^{-1}) and lifetimes τ in Al-like and Si-like xenon ions. The lifetimes of levels that have only E1-forbidden decay channels (ground configuration and one excited level in each ion) are much longer than the others; their lifetime is noted as $a(b) = a \times 10^b$ ps.

State	Al-like		State	Si-like	
	E (cm^{-1})	τ (ps)		E (cm^{-1})	τ (ps)
$3s^2 3p^2 \text{}^2\text{P}_{1/2}^o$	0		$3s^2 3p^2 \text{}^3\text{P}_0$	0	
$3s^2 3p^2 \text{}^2\text{P}_{3/2}^o$	667 574	3.79(5)	$3s^2 3p^2 \text{}^3\text{P}_1$	595 487	3.64(5)
$3s 3p^2 \text{}^4\text{P}_{1/2}$	817 897	87.0	$3s^2 3p^2 \text{}^3\text{P}_2$	646 721	8.29(7)
$3s 3p^2 \text{}^4\text{P}_{3/2}$	1343 238	796	$3s^2 3p^2 \text{}^1\text{D}_2$	1279 395	1.99(5)
$3s 3p^2 \text{}^4\text{P}_{5/2}$	1433 127	202	$3s^2 3p^2 \text{}^1\text{S}_0$	1391 729	1.37(5)
$3s 3p^2 \text{}^2\text{P}_{3/2}$	1557 533	11.0	$3s 3p^3 \text{}^5\text{S}_2^o$	1417 831	117
$3s 3p^2 \text{}^2\text{P}_{1/2}$	1622 936	2.92	$3s 3p^3 \text{}^3\text{D}_1^o$	1577 544	10.4
$3s^2 3d^2 \text{}^2\text{D}_{3/2}$	1916 301	2.22	$3s^2 3p 3d^3 \text{}^3\text{D}_2^o$	1779 932	716
$3s^2 3d^2 \text{}^2\text{D}_{5/2}$	1963 221	82.2	$3s 3p^3 \text{}^3\text{D}_2^o$	1917 844	534
$3s 3p^2 \text{}^2\text{D}_{5/2}$	2161 052	5.11	$3s^2 3p 3d^3 \text{}^3\text{D}_3^o$	1979 153	94.4
$3s 3p^2 \text{}^2\text{S}_{1/2}$	2292 721	4.16	$3s^2 3p 3d^3 \text{}^3\text{D}_1^o$	1994 272	1.65
$3s 3p^2 \text{}^2\text{D}_{3/2}$	2332 373	2.11	$3s^2 3p 3d^3 \text{}^1\text{D}_2^o$	2106 886	6.01
$3p^3 \text{}^4\text{S}_{3/2}^o$	2391 645	9.92	$3s 3p^3 \text{}^3\text{D}_3^o$	2128 563	12.4
$3s 3p 3d^2 \text{}^2\text{D}_{3/2}^o$	2503 658	28.4	$3s 3p^3 \text{}^3\text{P}_0^o$	2162 316	13.0
$3s 3p 3d^2 \text{}^2\text{D}_{5/2}^o$	2564 648	110	$3s 3p^3 \text{}^3\text{P}_1^o$	2226 461	7.41
$3s 3p 3d^4 \text{}^2\text{D}_{1/2}^o$	2705 035	2.93	$3s 3p^3 \text{}^3\text{P}_2^o$	2257 252	4.17
$3s 3p 3d^4 \text{}^2\text{D}_{3/2}^o$	2714 275	3.03	$3s 3p^3 \text{}^3\text{S}_1^o$	2309 977	2.22
$3s 3p 3d^4 \text{}^2\text{D}_{5/2}^o$	2727 239	12.2	$3s^2 3p 3d^3 \text{}^3\text{P}_2^o$	2584 398	1.61
$3s 3p 3d^4 \text{}^2\text{D}_{7/2}^o$	2776 926	21.0	$3s^2 3p 3d^3 \text{}^3\text{F}_2^o$	2585 651	71.8
$3s 3p 3d^2 \text{}^2\text{D}_{5/2}^o$	2834 659	12.1	$3s^2 3p 3d^3 \text{}^3\text{F}_3^o$	2587 049	2.60
$3s 3p 3d^2 \text{}^2\text{D}_{3/2}^o$	2840 974	4.68	$3s^2 3p 3d^3 \text{}^3\text{P}_1^o$	2587 761	1.95
$3s 3p 3d^2 \text{}^2\text{F}_{5/2}^o$	3057 098	5.26	$3s^2 3p 3d^3 \text{}^3\text{F}_4^o$	2593 372	4.29(5)
$3p^3 \text{}^2\text{F}_{3/2}^o$	3105 346	2.31	$3s^2 3p 3d^3 \text{}^3\text{P}_0^o$	2599 675	2.25
$3p^3 \text{}^2\text{P}_{1/2}^o$	3134 007	3.79	$3s 3p^2 3d^5 \text{}^5\text{F}_1$	2619 663	55.7
$3s 3p 3d^4 \text{}^2\text{F}_{3/2}^o$	3254 258	3.64	$3s 3p^2 3d^5 \text{}^5\text{F}_2$	2650 610	58.7
$3s 3p 3d^4 \text{}^2\text{F}_{5/2}^o$	3256 826	2.93	$3s^2 3p 3d^3 \text{}^1\text{F}_3^o$	2796 197	3.84
$3s 3p 3d^4 \text{}^2\text{P}_{1/2}^o$	3260 609	4.16	$3s^2 3p 3d^3 \text{}^1\text{P}_1^o$	2821 938	5.56
$3s 3p 3d^4 \text{}^2\text{F}_{7/2}^o$	3273 673	4.45	$3s 3p^2 3d^5 \text{}^5\text{D}_3$	2825 716	18.3
$3s 3p 3d^4 \text{}^2\text{F}_{9/2}^o$	3290 408	4.64(5)	$3s 3p^2 3d^5 \text{}^5\text{D}_2$	2884 305	17.6
$3s 3p 3d^4 \text{}^2\text{P}_{3/2}^o$	3389 679	3.92	$3s 3p^3 \text{}^1\text{D}_2^o$	2905 186	2.66
$3s 3p 3d^4 \text{}^2\text{P}_{5/2}^o$	3421 967	5.69	$3s 3p^3 \text{}^1\text{P}_1^o$	3047 160	1.61
$3s 3p 3d^2 \text{}^2\text{P}_{3/2}^o$	3483 350	2.37	$3s 3p^2 3d^5 \text{}^5\text{P}_2$	3085 628	12.0
$3s 3p 3d^2 \text{}^2\text{F}_{7/2}^o$	3498 082	5.67	$3s 3p^2 3d^5 \text{}^5\text{D}_0$	3120 579	44.9
$3s 3p 3d^2 \text{}^2\text{F}_{5/2}^o$	3525 761	1.74	$3s 3p^2 3d^5 \text{}^5\text{D}_1$	3139 253	83.2
$3p^2 3d^4 \text{}^4\text{F}_{3/2}$	3528 947	11.7	$3s 3p^2 3d^5 \text{}^5\text{F}_3$	3162 322	56.9
$3s 3p 3d^2 \text{}^2\text{P}_{1/2}^o$	3540 680	1.75	$3s 3p^2 3d^5 \text{}^5\text{D}_4$	3232 268	179
$3s 3p 3d^2 \text{}^2\text{F}_{7/2}^o$	3588 466	3.30	$3s 3p^2 3d^5 \text{}^5\text{F}_4$	3271 090	667
			$3s 3p^2 3d^5 \text{}^5\text{F}_5$	3376 651	133

Table 2 comprises a few levels for Al- and Si-like Xe ions with lifetimes that are several orders of magnitude longer than the others. These are levels that cannot decay via E1 transitions, but only by higher-multipole order radiation, like M1, E2 or M2. Such long-drawn out decays play no role in the present (time-resolved) beam–foil spectra. They would be

Table 3. Strongest E1 decay lines and transition probabilities A in xenon ions in the wavelength range 50–110 Å. The upper levels are selected with lifetimes τ larger than 15 ps to simulate delayed measurements. The Roman numeral labels in the first column refer to the spectral features in figures 1 and 2. The elemental symbols Ne, Na, Mg, Al and Si denote the isoelectronic sequences.

Label	λ (Å)	Upper level	τ (ps)	Lower level	A (s^{-1})	$A^2\tau$	
I	52.155	$3s3p3d\ ^4P_{1/2}^o$	4.156	$3s3p^2\ ^4P_{3/2}$	2.27(11)	2.15(11)	Al
	52.184	$3s^23d\ ^2D_{3/2}$	2.215	$3s^23p\ ^2P_{1/2}^o$	4.51(11)	4.51(11)	Al
	52.258	$3s3p3d\ ^4F_{5/2}^o$	2.930	$3s3p^2\ ^4P_{3/2}$	1.01(11)	3.01(10)	Al
	52.328	$3s3p3d\ ^4F_{3/2}^o$	3.639	$3s3p^2\ ^4P_{3/2}$	2.19(11)	1.74(11)	Al
II	54.834	$3s3p3d\ ^4F_{5/2}^o$	2.930	$3s3p^2\ ^4P_{5/2}$	2.24(11)	1.47(11)	Al
	55.180	$3p^2\ ^3P_2$	3.960	$3s3p\ ^3P_1^o$	2.50(11)	2.47(11)	Mg
III	58.285	$3d\ ^2D_{3/2}$	5.785	$3p\ ^2P_{1/2}^o$	1.66(11)	1.59(11)	Na
IV	60.924	$2p_{1/2}^{-1}3d_{3/2}\{2\}$	7.011	$2p_{1/2}^{-1}3p_{1/2}\{1\}$	1.38(11)	1.33(11)	Ne
	61.465	$3s3p^2\ ^2S_{2/1}$	4.161	$3s^23p\ ^2P_{3/2}^o$	2.36(11)	2.31(11)	Al
	61.509	$2p_{3/2}^{-1}3d_{3/2}\{3\}$	7.184	$2p_{3/2}^{-1}3p_{1/2}\{2\}$	1.34(11)	1.30(11)	Ne
	61.617	$3s3p^2\ ^2P_{1/2}$	2.915	$3s^23p\ ^2P_{1/2}^o$	3.30(11)	3.18(11)	Al
V	61.833	$2p_{3/2}^{-1}3d_{3/2}\{1\}$	1.274	$2p_{3/2}^{-1}3p_{1/2}\{1\}$	1.07(11)	1.45(10)	Ne
	62.916	$3p^2\ ^3P_1$	4.706	$3s3p\ ^3P_0^o$	1.19(11)	6.71(10)	Mg
	62.917	$3s3p\ ^1P_1^o$	3.645	$3s^2\ ^1S_0$	2.74(11)	2.74(11)	Mg
	63.682	$2p_{3/2}^{-1}3d_{3/2}\{0\}$	7.941	$2p_{3/2}^{-1}3p_{1/2}\{1\}$	1.23(11)	1.21(11)	Ne
	63.823	$3s3p^3\ ^3P_0^o$	12.98	$3s^23p^2\ ^3P_1$	7.70(10)	7.70(10)	Si
	64.059	$3p^23d\ ^4F_{7/2}^o$	6.648	$3s3p3d\ ^4F_{5/2}^o$	1.15(11)	8.74(10)	Al
	64.204	$3s3p^2\ ^2P_{3/2}$	10.96	$3s^23p\ ^2P_{1/2}^o$	8.39(10)	7.71(10)	Al
	64.807	$3s3p^23d\ ^5D_0$	44.90	$3s3p^3\ ^3D_1^o$	1.79(10)	1.44(10)	Si
VI	66.102	$3p^2\ ^1D_2$	13.08	$3s3p\ ^3P_1^o$	5.70(10)	4.25(10)	Mg
	66.631	$3p\ ^2P_{3/2}^o$	7.363	$3s^2P_{1/2}$	1.57(11)	1.57(11)	Na
	66.877	$3s3p3d\ ^2D_{5/2}^o$	5.107	$3s^23p\ ^2P_{3/2}^o$	1.96(11)	1.96(11)	Al
VII	75.958	$3s3d\ ^3D_3$	11.63	$3s3p\ ^3P_2^o$	8.60(10)	8.60(10)	Mg
VIII	78.988	$3p3d\ ^3F_3^o$	16.53	$3p^2\ ^1D_2$	3.15(10)	1.64(10)	Mg
IX	84.930	$3d\ ^2D_{5/2}$	15.34	$3p\ ^2P_{3/2}^o$	6.52(10)	6.52(10)	Na
X	87.027	$3d^2\ ^1G_4$	7.077	$3p3d\ ^1F_3$	1.02(11)	7.39(10)	Mg
XI	91.433	$2p_{1/2}^{-1}3d_{5/2}\{2\}$	18.56	$2p_{1/2}^{-1}3p_{3/2}\{1\}$	4.37(10)	3.55(10)	Ne
	91.454	$2p_{3/2}^{-1}3d_{5/2}\{3\}$	19.10	$2p_{3/2}^{-1}3p_{3/2}\{2\}$	4.04(10)	3.11(10)	Ne
	91.502	$2p_{1/2}^{-1}3d_{5/2}\{3\}$	20.09	$2p_{1/2}^{-1}3p_{3/2}\{2\}$	4.94(10)	4.91(10)	Ne
	93.333	$2p_{3/2}^{-1}3d_{5/2}\{4\}$	21.49	$2p_{3/2}^{-1}3p_{3/2}\{3\}$	4.65(10)	4.65(10)	Ne

expected, however, to contribute to low-density plasma spectra from a tokamak or an electron beam ion trap.

4.1. Comparison with Xe beam-foil spectra

The 1995 beam-foil spectra [8] mostly cover three spectral sections within the wavelength range from 50–150 Å. The spectra have been recorded at various foil displacements (up to 28 positions) from the line of sight of the spectrometer, corresponding to observations in a range of delays after excitation. In the short-wavelength parts (50–100 Å), the results for decays with level lifetimes longer than 2 ps are listed in table 3; in the longer-wavelength part (100–150 Å), the typical level lifetimes are also longer, and we have listed decays with characteristic lifetimes longer than 15 ps in table 4. Of the thousands of calculated lines that fall into the range 50–150 Å, we have listed only the strongest E1 lines expected. The observed

Table 4. Strongest E1 decay lines and transition probabilities A in xenon ions in the wavelength range 110–150 Å. The upper levels are selected with lifetimes larger than 15 ps to simulate delayed measurements. The numbers in the first column refer to the lines in figure 3. The elemental symbols F, Ne, Na, Mg, Al, Si and P denote the isoelectronic sequences.

No	λ (Å)	Upper level	τ (ps)	Lower level	A (s^{-1})	$A^2\tau$	
1	110.093	$3p^2\ ^3P_0$	14.67	$3s3p\ ^3P_1^o$	6.82(10)	6.81(10)	Mg
2	114.853	$3s3p^2d\ ^5F_2$	58.67	$3s3p^3\ ^3D_1^o$	7.12(09)	2.98(09)	Si
3	117.396	$3p3d\ ^3F_3^o$	16.07	$3s3d\ ^3D_3$	1.28(10)	2.70(09)	Mg
4	119.086	$3s3p^23d\ ^5F_1$	55.74	$3s3p^3\ ^3D_2^o$	9.48(09)	5.01(09)	Si
5	120.261	$3s3p^33d\ ^6D_{9/2}^o$	88.27	$3s^23p^23d\ ^4D_{7/2}$	8.15(09)	5.86(09)	P
6	121.604	$3s3p^3\ ^5S_2^o$	116.9	$3s^23p^2\ ^3P_1$	4.99(09)	2.91(09)	Si
7	122.265	$3s3p^2\ ^4P_{1/2}$	96.63	$3s^23p\ ^2P_{1/2}^o$	1.15(10)	1.15(10)	Al
8	123.937	$3p\ ^2P_{1/2}^o$	42.70	$3s^2S_{1/2}$	2.34(10)	2.34(10)	Na
9	127.668	$3s3p^23d\ ^5F_5$	132.7	$3s^23p3d\ ^3F_4^o$	7.53(09)	7.53(09)	Si
10	129.683	$3s3p^3\ ^5S_2^o$	116.9	$3s^23p^2\ ^3P_2$	3.56(09)	1.49(09)	Si
10	129.953	$3s3p\ ^3P_1^o$	160.54	$3s^2\ ^1S_0$	6.16(09)	6.16(09)	Mg
11	130.318	$3s3p^2\ ^4P_{3/2}$	184.99	$3s^23p\ ^2P_{3/2}^o$	4.95(09)	4.95(09)	Al
12	132.262	$3p3d\ ^3F_2^o$	34.15	$3s3d\ ^3D_1$	1.01(10)	3.55(09)	Mg
13	133.945	$2p_{1/2}^{-1}3p_{1/2}\{1\}$	56.97	$2p_{1/2}^{-1}3s_{1/2}\{1\}$	9.87(09)	5.54(09)	Ne
13	133.991	$2p_{3/2}^{-1}3p_{1/2}\{1\}$	57.86	$2p_{3/2}^{-1}3s_{1/2}\{2\}$	1.56(10)	1.40(10)	Ne
14	134.768	$2p_{1/2}^{-1}3p_{1/2}\{1\}$	56.97	$2p_{1/2}^{-1}3s_{1/2}\{0\}$	5.81(09)	1.92(09)	Ne
15	138.554	$2p_{3/2}^{-1}3p_{1/2}\{2\}$	56.28	$2p_{3/2}^{-1}3s_{1/2}\{1\}$	8.15(09)	3.73(09)	Ne
16	139.999	$2p^43p\ ^4P_{1/2}^o$	76.05	$2p^43s^2D_{3/2}$	5.29(09)	2.13(09)	F
17	141.375	$2p^43p\ ^4D_{5/2}^o$	76.12	$2p^43s^4P_{5/2}$	7.38(09)	4.15(09)	F
18	145.606	$2p^43p\ ^4P_{3/2}^o$	29.86	$2p^43s^4P_{5/2}$	1.09(10)	3.54(09)	F
19	147.554	$3s3p^23d\ ^3F_4$	667.0	$3s^23p3d\ ^3F_4^o$	1.04(09)	7.25(08)	Si
19	147.609	$3s3p^2\ ^4P_{3/2}$	795.8	$3s^23p\ ^2P_{3/2}^o$	7.18(09)	4.10(08)	Al

spectra show much fewer lines; considering the predicted line spacings and the experimental spectral resolution, it is likely that many of the observed lines represent line blends.

In order to facilitate the visual comparison of calculated atomic data with observations, we have synthesized spectra on the basis of our calculations. Line intensities were estimated from transition probabilities and corrected for branch fractions; for the matching of delayed spectra, the atomic decays were followed over a corresponding time interval. For the superposition of spectra from ions in different charge states, the charge state fractions were modified somewhat to improve the visual agreement of predicted and observed spectra. This charge state distribution (close to the experimental estimates) was the only free parameter; the *ab initio* calculational results for the wavelengths were not altered. No explicit attempt was made to set up a model of initial level populations and cascade repopulation from high-lying levels. Especially with the non-selective ion–foil interaction, high-lying and even multiply excited levels may be populated, and cascade tails play a significant role in the decay curve analysis of few-electron ions. Collisional-radiative models (like those based on the HULLAC [67, 68] or the FAC code [69]) specialize in such multilevel population dynamics, but they do not necessarily reach our wavelength accuracy. Because of the coarse modelling, the relative line intensities in our synthetic spectra ought to be taken with a grain of salt.

In earlier experimental studies, line identifications have often been guided by multi-configuration Hartree–Fock (MCHF) or multi-configuration Dirac–Fock (MCDF) calculations, as was the case in the 1995 study of the beam–foil spectra [8]. Typically the MCDF wavelengths deviate from experiment by as much as 2 Å; such a deviation causes uncertainty with the line identifications in line-rich spectra like the present ones.

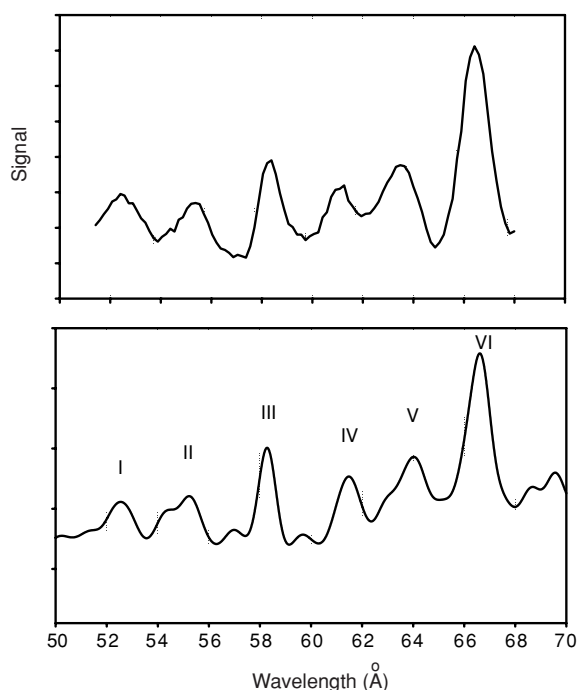


Figure 1. Experimental (top) and synthetic (bottom) spectra of xenon ions in the wavelength range 50–70 Å. The upper trace shows replotted beam–foil data of [7, 8], the lower one results from our present calculations. Na, Mg, and Al denote the isoelectronic sequences of the corresponding Xe lines. Approximate charge state fractions: F-like ions 0.05, Ne-like 0.10, Na-like 0.55, Mg-like 0.20, Al-like 0.12, Si-like 0.05 and P-like 0.01. Branching was accounted for. Simulated for a delay time of 10 ps.

Figures 1 and 2 show new lineouts of the beam–foil spectra first presented in [8], now with improved wavelength scales. Figure 3 also shows data from that experiment, but is constructed from a different set of observations that had higher spectral resolution (but fewer foil positions which would be needed for lifetime studies). The three figures also contain synthetic spectra of the same spectral ranges, simulated for an appropriate delay time after excitation. The lines marked in figures 1 and 2 are identified in table 3. Figure 3 compares a synthetic spectrum based on nineteen theoretical E1 lines (numbered 1–19 in table 4) with the experimental beam foil spectrum in the 110–150 Å range.

The long-wavelength section of the experimental beam–foil data (mostly featuring $3s-3p_{1/2}$ transitions) was basically correctly displayed in [8]. The middle section, with the $3p_{3/2}-3d_{5/2}$ transition in Na-like Xe (84.93 Å) as an anchor, required a slight rescaling of the dispersion; it now shows a striking likeness to the synthetic spectrum (see figure 3) which in turn lends credibility to the calculated values and to the thus available identifications of the weak lines in this range (table 4).

The short-wavelength section of the beam–foil spectra required a massive correction to the assumed spectral dispersion. With the wavelength anchor unchanged (the $3p_{1/2}-3d_{3/2}$ transition in Na-like Xe (58.285 Å)), the corrected dispersion points to a different line than before as the Mg-like Xe resonance transition $3s^2\ ^1S_0-3s3p\ ^1P_1^o$ (62.917 Å). The strongest line of the spectrum was previously found to coincide with the prediction for a line in Ne-like

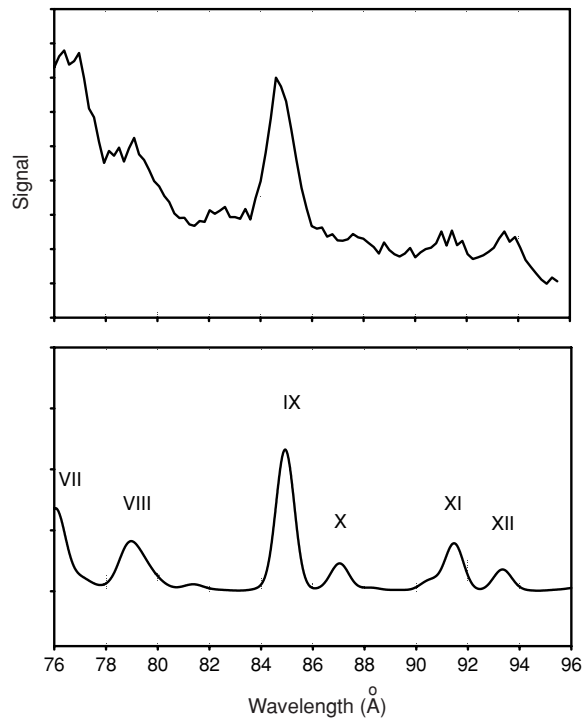


Figure 2. Experimental beam-foil (replotted data of [7, 8]) (top) and synthetic (bottom) spectra of xenon ions in the wavelength range 76–96 Å. Approximate charge state fractions: F-like ions 0.05, Ne-like 0.10, Na-like 0.55, Mg-like 0.20, Al-like 0.12, Si-like 0.05 and P-like 0.01. Branching was accounted for. Simulated for a delay time of 10 ps.

Xe (see [8]). Now given a wavelength of near 66.5 Å, this line turns out to comprise several lines that may be expected to be strong, among them the $3s_{1/2}-3p_{3/2}$ transition in the Na-like Xe ion (66.631 Å). (The line in the Ne-like ion is still present, as part of a cluster of weak lines, at 68.733 Å.) The aforementioned transition in the Na-like ion on its own cannot explain the overall intensity of the line (although cascade repopulation would easily boost the line intensity beyond the result of our calculations); an important blending partner is the $3s3p\ ^1P_1^o-3p^2\ ^1D_2$ transition in the Mg-like ion (66.102 Å), which also carries massive cascade repopulation along the chain of yrast levels (that is, of high n , maximum l levels). In low- Z ions, the $3p^2\ ^1D_2$ level lifetime is about four to five times as long as the $3s3p\ ^1P_1^o$ level lifetime. In higher- Z ions, however, a decay channel of the $3p^2\ ^1D_2$ level to the $3s3p\ ^1P_{1,2}^o$ levels opens up and progressively shortens the 1D_2 level lifetime (see discussion in [70–72]). For Mg-like Xe, the expected lifetime ratio is only about a factor of two, from an about equal branching of the 1D_2 level decays into branches without and with spin change.

There are several interesting observations in the long-wavelength range spectrum. MCDF calculations [58, 60] predict that Al-like ion $3s^23p\ ^2P_{3/2}^o-3s3p^2\ ^4P_{5/2}$ and Si-like ion $3s^23p^2\ ^3P_2-3s3p^3\ ^5S_2^o$ lines are blended at 128.95–128.96 Å. Therefore, Träbert *et al* [8] earlier identified the line at 127.9 ± 1.0 Å as a candidate for the Si-like ion $3s^23p^2\ ^3P_2-3s3p^3\ ^5S_2^o$ line and the 130.4 Å line as the blend of Mg-like and Al-like lines (labelled J and K in [8]). The results of our MR–MP calculations, however, suggest that their line J results from the decay of lowest even-parity $J = 5$ level in the Si-like ion to the lowest odd-parity $J = 4$ level,

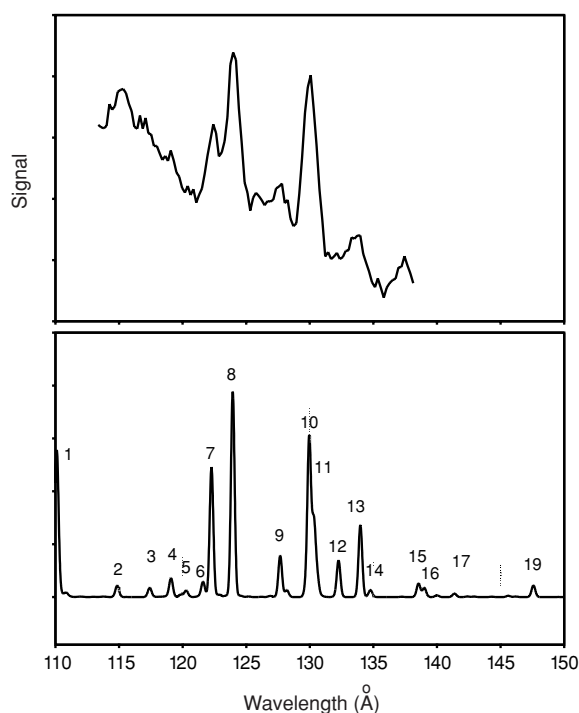


Figure 3. Experimental beam-foil data [7, 8] (top) and synthetic (bottom) spectra of xenon ions in the wavelength range 110–150 Å. Approximate charge state fractions: F-like ions 0.02, Ne-like 0.13, Na-like 0.32, Mg-like 0.35, Al-like 0.18, Si-like 0.08 and P-like 0.02. Branching was accounted for. Simulated for a delay time of 40 ps.

and not from the $^3P_2-^5S_2^0$ transition. The lower level of this particular transition, $3s^23p3d\ ^3F_4^0$, is also relatively long-lived. All of its decay branches are electric-dipole forbidden transitions. Because of its longevity (a level lifetime of about 10 ms has been measured in a storage ring experiment of Si-like Fe^{12+} ions [73]), it probably is quenched in many laboratory plasmas. Spectrally resolved observations of the decay branches do not exist, but the decay of the (not as long-lived) $^3F_3^0$ level of the same term has been identified in delayed beam-foil spectra of ions of iron group elements [74], in agreement with calculations of the same type as used here [22]. The new assignment refers to a transition not assigned (to our knowledge) in any other Si-like ion; hence there is no expertise and isoelectronic comparison to help judge the validity of the assignment, beyond our calculation and the supporting argument that in beam-foil spectra the levels with the highest J -values often are amply populated. However, such particularly long-lived levels far above the ground configuration do occur in quite a number of isoelectronic sequences (for an early discussion, see [75]). They contribute to extended cascade tails in beam-foil lifetime measurements, and they may be of importance in the diagnostics of plasma spectra where they influence the temporal development of discharges by providing excited-level population traps with level lifetimes that differ from most of the neighbouring levels by several orders of magnitude. Their longevity may also provide stepping stones for collisional ionization well below the ionization potential of a given ion, and thus they influence the charge state balance [76]. Beyond the ground configuration that has M1 and E2 transitions only, table 2 lists one excited level each in Al-like and Si-like ions that has no electric dipole decays and therefore has a much longer lifetime.

Within the experimental uncertainty, the strong lines of the Na- and Mg-like ions were seen in the beam–foil spectra at positions that agreed with preceding measurements on stationary light sources. (A typesetting error occurred in table 1 of [8]: a line (actually a line blend) at 130.4 Å (old calibration) (see figure 3) was wrongly listed with a wavelength of 134 Å). The observed positions of the transitions in Na-like ions at 123.9 ± 0.5 Å, Mg-like ions at 63.2 ± 0.5 Å and at 130.4 ± 0.5 Å, and of the Al-like ion 122.5 ± 0.5 Å and 147.0 ± 1.0 Å lines agree with the MR–MP prediction within the experimental error. However, the identification of the Al-like 122.5 ± 0.5 Å line, $^4P_{1/2} - ^2P_{3/2}^o$, ought to read ($^4P_{1/2} - ^2P_{1/2}^o$). The predicted Si-like ion $^3P_1 - ^5S_2^o$ line at 121.604 Å is blended with the Al-like ion line $^2P_{1/2}^o - ^4P_{1/2}$ at 122.265 Å. The predicted Si-like ion $^3P_2 - ^5S_2^o$ line at 129.683 Å is blended with other lines at 130 Å.

Because of the blending situation and the charge state distribution, there is no direct observation of the two decay branches of the $3s3p^3\ ^5S_2^o$ level in the Si-like ion, invalidating the tentative suggestion made in the earlier work [8], then guided by a survey calculation [60]. Bengtsson *et al* [62] have declared that suggestion to be anyway grossly wrong, based on their isoelectronic studies that showed a trend which, however, itself deviated noticeably from the well-established trend at lower nuclear charges [59]. When this inconsistency was pointed out [63], Ishikawa and Vilkas [64] performed new calculations which indicated that probably everybody had been not quite right on these transitions in high-*Z* Si-like ions (Xe and Au [8, 9]) so far. Another later calculation [65] has wavelength results near to the same isoelectronic trend, but it does not mention any corrections for radiative effects. Obviously, the level position and decay details of the lowest quintet levels in Si-like ions in the middle of the periodic table of elements cannot be sorted out without high-resolution spectra of several ions (isoelectronic trends), and these are not yet available.

4.2. Comment on decay curves and lifetimes

One of the unique advantages of the beam–foil light source lies in the fact that it inherently provides time resolution and thus can be used to determine atomic level lifetimes in the picosecond- to nanosecond-range. This property was the main point of [7, 8]. At the time it was noted that several lines consisted of line blends, representing the decays of levels with not very different lifetimes (similar electronic states in ions that differ by one or a few units of charge). The new calculations indicate that even more decays may have contributed.

For example, there are four major $3s-3p-3d$ transitions in the Na-like Xe ion, and previous beam–foil work [7] found them in a pattern of decay curves and extracted lifetimes that were compatible with expectation, although we now know that one of the four lines was misidentified. Similarly, the resonance line in the Mg-like ion was misidentified, but the measured lifetime is in reasonable accord with expectation. The reason for the overall agreement of experiment and calculation lies in the ‘type of transition’. The lines in the spectra are grouped by ‘type’: in Xe, the $3s_{1/2}-3p_{1/2}$ lines have about twice the wavelength of the $3s_{1/2}-3p_{3/2}$ lines; within each ‘type’, the wavelength (and thus lifetime) differences are small, because the screening differences in Na-, Mg- and Al-like ions are small, while some of the oscillator and line strength values are practically the same. Where the spin changes (intercombination transitions), as in the $3s_{1/2}-3p_{1/2}$ transitions of Mg- and Al-like ions, the predicted lifetimes differ by only 10%—which is quite compatible with the experimental uncertainty. In table 5 we present the previously reported lifetime measurement results in combination with the updated line identifications.

The Mg-like ion line $^1S_0 - ^3P_1^o$ at 129.95 Å, the Al-like ion line at 130.32 Å and the Si-like ion line at 129.68 Å are blended. The theoretical MR–MP lifetime value of 160.5 ps for the Mg $^3P_1^o$ level is in good agreement with the MBPT lifetime of 163 ps. These theoretical lifetimes

Table 5. Beam-foil lifetimes [7, 8] and updated Xe line identifications. The elemental symbols Ne, Na, Mg, Al and Si denote the isoelectronic sequences. Wavelength and lifetime values marked with an asterisk (*) are from this work. Wavelengths of transitions in Na-like ions have been used as references and are therefore give without error bars.

Wavelength λ (nm)		Sequence and transition	Lifetime τ (ps)	
Observed	Reference		Observed	Predicted
58.2	58.229 [40]	Na 3d $^2D_{3/2} \rightarrow 3p \ ^2P_{1/2}^0$	6 ± 1.2	5.62 [49, 17]
	58.285*			5.79*
61.3 ± 0.3			5 ± 1.5	
	60.924*	Ne 2p $_{1/2}^{-1}3d_{3/2}\{2\} \rightarrow 2p_{1/2}^{-1}3p_{1/2}\{1\}$		7.01*
	61.465*	Al 3s3p $^2 \ ^2S_{1/2} \rightarrow 3s^23p \ ^2P_{3/2}^0$		4.16*
	61.509*	Ne 2p $_{3/2}^{-1}3d_{3/2}\{3\} \rightarrow 2p_{3/2}^{-1}3p_{1/2}\{2\}$		7.18*
	61.617*	Al 3s3p $^2 \ ^2P_{1/2} \rightarrow 3s^23p \ ^2P_{1/2}^0$		2.92*
	61.833*	Ne 2p $_{3/2}^{-1}3d_{3/2}\{1\} \rightarrow 2p_{3/2}^{-1}3p_{1/2}\{1\}$		1.27*
63.8 ± 0.5	62.895 [42]	Mg 3s3p $^1P_1^0 \rightarrow 3s^2 \ ^1S_0$	6.8 ± 0.6	3.54 [51]
	72.14 [52]			3.21 [55]
	62.916*			4.71*
	63.682*	Ne 2p $^53p \ ^3P_0 \rightarrow 2p^53s^3P_1^0$		7.94*
	63.823*	Si 3s3p $^3 \ ^3P_0^0 \rightarrow 3s^23p^2 \ ^3P_1$		13.0*
	64.059*	Al 3p $^23d \ ^4F_{7/2}^0 \rightarrow 3s3p3d \ ^4F_{5/2}^0$		6.65*
	64.204*	Al 3s3p $^2 \ ^2D_{3/2} \rightarrow 3s^23p \ ^2P_{1/2}^0$		11.0*
	66.102*	Mg 3p $^2 \ ^1D_2 \rightarrow 3s3p^3P_1^0$		13.1*
66.5	66.541 [40]	Na 3p $^2P_{3/2}^0 \rightarrow 3s^2S_{1/2}$	14 ± 1.5	6.27 [49, 17]
	66.631*			7.36
	66.877*	Al 3s3p3d $^2D_{5/2}^0 \rightarrow 3s^23p \ ^2P_{3/2}^0$		5.11*
84.8	84.814 [40]	Na 3d $^2D_{5/2} \rightarrow 3p \ ^2P_{3/2}^0$	14 ± 4	14.9 [49]
				15 [17]
	84.930*			15.3*
120 ± 0.1				
	120.65 [60]	Si 3s3p $^3 \ ^5S_2^0 \rightarrow 3s^23p^2 \ ^3P_1$		111 [60]
	121.604*			117*
122.4 ± 0.2	121.15 [58]	Al 3s3p $^2 \ ^4P_{1/2} \rightarrow 3s^23p \ ^2P_{1/2}^0$		83 [58]
	122.265*			96.6*
123.9	123.897 [40]	Na 3p $^2P_{1/2}^0 \rightarrow 3s^2S_{1/2}$	42 ± 3	42 [49, 17]
	123.937*			42.7*
127.9 ± 0.1	127.668*	Si 3s3p $^23d \ ^5F_5 \rightarrow 3s^23p3d \ ^3F_4^0$		133*
	128.95 [60]	Si 3s3p $^3 \ ^5S_2^0 \rightarrow 3s^23p^2 \ ^3P_2$		111 [60]
	129.683*			117*
	128.96 [58]	Al 3s3p $^2 \ ^4P_{5/2} \rightarrow 3s^23p \ ^2P_{3/2}^0$		191 [58]
	130.318*			185*
130.0 ± 0.1	129.92 [42]	Mg 3s3p $^3P_1^0 \rightarrow 3s^2 \ ^1S_0$	170 ± 30	158 [51]
	129.92 [52]			153 [55]
	129.953*			161
133.3 ± 0.3				
	146.3 [58]	Al 3s3p $^2 \ ^4P_{3/2} \rightarrow 3s^23p \ ^2P_{3/2}^0$		762 [58]
	147.609*			796*

are in good agreement with the experimental lifetime of 170 ± 30 ps within the experimental uncertainty.

While in some cases the lifetime data can be associated with one dominant contribution to the effective decay curve obtained from a spectral feature, there are other features that

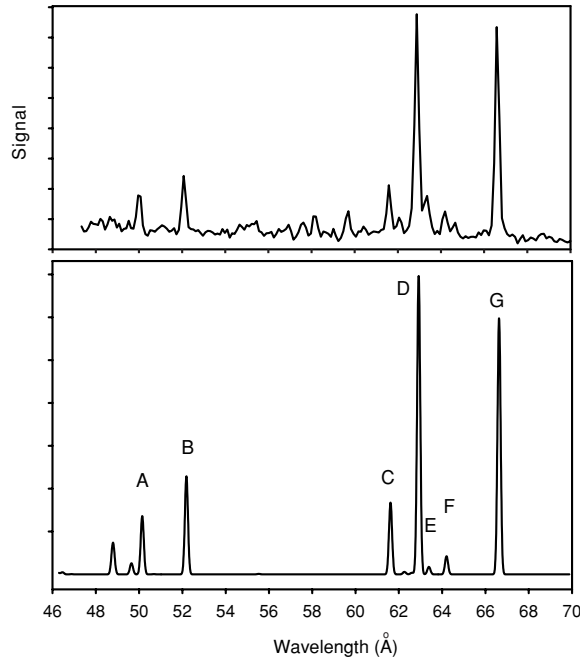


Figure 4. Section of a Xe spectrum obtained at an electron beam ion trap [10] (top) and corresponding synthetic spectrum (bottom). The spectrometer has a similar Rowland circle diameter ($R = 5$ m) as the one used for the beam-foil spectra shown in figures 1–3, but has a four times higher groove density. The gain in spectral resolving power is striking. The principal spectral features in this spectrum are identified in table 6.

consist of too many blended components to ascribe the result of multiexponential fits to just one level. The measurements agree with expectation in all cases at least in the sense that in the short-wavelength spectral section the typical lifetimes of interest are near 10 ps, and that lifetimes of about 100 to 200 ps in the long-wavelength spectra. However, in order to obtain more level-specific lifetime numbers from experiment, measurements with higher spectral resolution are required. The same is necessary to find out about the relative importance of various calculated contributions to a given spectral feature.

4.3. Comparison with recent Xe spectra from the Livermore electron beam ion trap

For need of signal, grating spectrometers in beam-foil spectroscopy usually operate with much wider slits than would be possible at the diffraction limit. Under such conditions, the line width is dominated by the instrumental line width and is largely independent of wavelength. This implies that at short wavelengths the resolving power $\lambda/\Delta\lambda$ suffers. This is evident in the beam-foil spectra that we show. Higher resolving power would be available, if the Doppler broadening was reduced (for example, by using a stationary light source instead of the fast ion beam), or a grating with a larger Rowland circle radius or of higher groove density. As it happens, there are data available from an electron beam ion trap (Livermore SuperEBIT, a stationary light source) that have been obtained with a grating of similar Rowland circle size (diameter 5 m) and a groove density of $1200 \text{ } \ell \text{ mm}^{-1}$ (four times higher than in the GSI work) [10]. These spectra include the range from 50–70 Å (figure 4, table 6). The EBIT spectra cover the other ranges of the beam-foil data set, too. For example, they show the strong lines

Table 6. EBIT spectrum of xenon ions. The letter labels refer to spectral features in figure 4. Experimental wavelength uncertainties are about 0.05 Å. The elemental symbols Na, Mg, Al and Si denote the isoelectronic sequences.

Label	λ_{expt}	λ_{theor}	Upper level	τ (ps)	Lower level	A (s^{-1})	$A^2\tau$	
A	50.03	50.144	$3s3p^3\ ^1P_1^o$	1.648	$3s^23p^2\ ^3P_0$	6.03(11)	5.99(11)	Si
B	52.07	52.184	$3s3p^2\ ^2D_{3/2}$	2.215	$3s^23p\ ^2P_{1/2}^o$	4.51(11)	4.51(11)	Al
C	61.58	61.617	$3s3p^2\ ^2P_{1/2}$	2.915	$3s^23p\ ^2P_{1/2}^o$	3.30(11)	3.18(11)	Al
D	62.88	62.917	$3s3p\ ^1P_1^o$	3.645	$3s^2\ ^1S_0$	2.74(11)	2.74(11)	Mg
E	63.35	63.390	$3s3p^3\ ^3D_1^o$	10.38	$3s^23p^2\ ^3P_0$	7.87(10)	6.43(10)	Si
F	64.19	64.204	$3s3p^2\ ^2P_{3/2}$	10.96	$3s^23p\ ^2P_{1/2}^o$	8.39(10)	7.71(10)	Al
G	66.60	66.631	$3p\ ^2P_{3/2}^o$	7.363	$3s^2S_{1/2}$	1.57(11)	1.57(11)	Na

of figure 4 also in second and third diffraction orders. However, the first diffraction order lines near 130 Å are very weak in those spectra, too weak to merit analysis in the present context.

The EBIT spectra in the 70 Å range are not calibrated to high precision, because the calibration emphasis in that work was on a different range within the operating range of the spectrometer. The spectrum shown in figure 4 is, in fact, from the short-wavelength edge of a spectrum in which the lines of present interest are covered only by an extrapolation of the calibration from the nearest reference points. The agreement of calculated wavelengths and observed spectral features nevertheless is typically better than 0.05 Å, which is also the estimated calibration uncertainty.

The relative line intensities in the EBIT spectrum are drastically different from those of the beam–foil spectra. Excitation in EBIT is (almost) from the true ground state only—this is typical for a low density light source in which there is sufficient time between excitations so that excited levels can decay radiatively before the next collisional excitation takes place. In the high-density environment inside an exciter foil (or in a laser-produced plasma), the collision frequency is so much higher that practically all levels can be reached. The beam–foil spectra are richer (more crowded). Consequently, line blends afflict the aforementioned beam–foil spectra much more than the EBIT spectra. However, our calculations indicate that the strong line of Na-like Xe in the EBIT spectrum, which may be considered as a wavelength anchor, may be suffering from a blend with a line from the P-like Xe ion, within its rather narrow line width. Even higher spectral resolution will be needed for an unambiguous spectral analysis and high-accuracy wavelength determinations. Table 6 identifies the prominent features of the EBIT spectrum according to our calculations and to [10].

5. Conclusion

In the present work we discuss how a series of calculations by a given technique fares on a range of ions of the same element, how spectral simulations can help in revealing assignment errors, and we reanalyse the earlier beam–foil data. In addition, we compare some of the synthetic spectra and the beam–foil data with observations from a light source of very different properties, the electron beam ion trap. Twelve years ago, it was difficult to find out, which strong line might be originating from which transition in which ion. With the new calculations, there are often several reasonable identifications within the measured line profile, and weak lines that have been neglected before can now be identified. Evidently, computations have remarkably improved. They clearly supersede some earlier theoretical work that had served as guidance for the spectral analysis of data beyond the range of nuclear charge Z for which a

Table 7. Contribution (cm^{-1}) from each order of perturbation theory to the transition energies of lines in the 60–150 Å wavelength region.

	E^{CI}	$E^{(2)}$	$E^{(0+1+2)\text{a}}$	E_{LS}^{b}	$E_{\text{other}}^{\text{c}}$	E_{total}
Na-like $3p\ ^2P_{1/2}^o-3s^2S_{1/2}$						
MR–MP	820 982	−2056	818 926	−11946	−62	806 862
MBPT ^d	830 667	−1633		−12217		806 817
Experiment [48]						806 970 ± 200
Mg-like $3s3p\ ^3P_1^o-3s^2\ ^1S_0$						
MR–MP	709 580	1030	710 610	−11493	−54	699 063
Mg-like $3s3p\ ^1P_1^o-3s^2\ ^1S_0$						
MR–MP	1606 498	−5578	1600 920	−10644	−833	1589 396
Experiment [10]						1590 460 ± 300
Experiment ^e						1590 330 ± 1250
Al-like $3s3p^2\ ^4P_{1/2}-3s^23p\ ^2P_{1/2}^o$						
MR–MP	830 114	−693	829 421	−11368	−103	817 897
Al-like $3s3p^2\ ^2P_{1/2}-3s^23p\ ^2P_{1/2}^o$						
MR–MP	1640 900	−6506	1634 394	−10589	−816	1622 936
Experiment ^e						1623 900 ± 1300
Si-like $3s3p^3\ ^3D_1^o-3s^23p^2\ ^3P_0$						
MR–MP	1589 544	−2225	1587 319	−8974	−748	1577 544
Experiment ^e						1578 500 ± 1250
Si-like $3s3p^3\ ^5S_2^o-3s^23p^2\ ^3P_1$						
MR–MP	833 204	164	833 368	−10917	−128	822 344
MR–MP [64]						822 701
RCI [65]			834 274			
Si-like $3s3p^3\ ^5S_2^o-3s^23p^2\ ^3P_2$						
MR–MP	779 846	2287	782 133	−10917	−126	771 110
MR–MP [64]						771 213
RCI [65]			782 234			

^a $E_K^{(0+1+2)} = E_K^{\text{CI}} + E_K^{(2)}$.^b Lamb shift correction.^c First-order frequency-dependent Breit correction, $\Delta B(w)^{(1)}$, plus normal and specific mass shifts.^d Third-order MBPT calculations [18] including Lamb shift corrections [17].^e Present work.

fairly consolidated body of atomic data existed at the time. The present calculations are the first that treat all Xe ion species of present interest on a comparable level of detail, and the wavelength results are good enough to enable instant line identifications with transitions in a fair range of ion charge states.

Now that the experimental data base has been clarified, we can compare the quality of our wavelength calculations with selected experimental data. Table 7 displays the contribution from each order of MR–MP perturbation theory to several representative transition energies in Na- to Si-like Xe ions. The relativistic CI energies E^{CI} (equation (6)) and second-order DCB correlation corrections $E^{(2)}$ (equation (18)) are displayed, respectively, in the second and third columns. The MR–MP transition energies are compared with experiment (where available) in the last column. Throughout the examples, theory agrees with experiment within the experimental uncertainty. Theory is in excellent agreement with experiment on the

prominent $3s-3p_{1/2}$ transition in Na-like Xe, which has been well characterized experimentally [48]. This agreement would not occur, however, if the QED contribution was not accounted for. Throughout the various Xe ions discussed here, the Lamb shifts result in significant corrections, of the order $10\,000\text{ cm}^{-1}$, and are needed to obtain close agreement between the calculated and experimental transition energies. The residual DCB correlation corrections are also non-negligible. An accurate account of the residual dynamic correlation by MR–MP is crucial in achieving spectroscopic accuracy even in the highly ionized high- Z ions.

The new calculations enhance and expand the interpretation of the available beam–foil spectra. They also predict the spectral features to be expected in adjacent spectral ranges. This is a most valuable practical tool for spectral exploration. A comparison with EUV spectra from an electron beam ion trap (which offers higher spectral resolution than the beam–foil technique, but has no comparable time resolution) reveals excellent agreement with the spectral structure seen in such an experiment. The EBIT spectra represent much more selective excitation features than does the ion–foil interaction, but the higher experimental precision obtainable, in combination with accurate calculations, seems to be superior to most spectral analyses based on the beam–foil technique alone.

The identification of almost all features in the line rich EUV spectra of, both, foil-excited Xe ion beams and the Xe ions stored in an electron beam ion trap, would have been almost impossible without detailed guidance by calculation. The present calculations appear to be not merely useful in this context; they are superior in wavelength accuracy to measurements that have not been trained to yield utmost wavelength accuracy (which likely can be achieved only under very favourable circumstances), and they actually compete with precise experiments. To put these claims into numbers: the deviation between our calculational results and experimentally established wavelengths for prominent lines in Na- and Mg-like Xe [40, 42] is of the order of 0.05 Å . We expect similar uncertainties for the other isoelectronic sequences, once experiment provides hard data. In contrast, the deviation of other calculations from our results (and thus most likely also from the proper experimental values) is ten to fifty times larger. Although the moderate spectral resolution of the beam–foil data is insufficient to resolve various line blends, the data rule out a number of earlier calculational results while being fully compatible with our calculations.

Acknowledgments

This research is supported in part by the US–Israel Binational Science Foundation. ET acknowledges travel support from the German Research Association (DFG). Part of this work has been performed at LLNL under the auspices of the USDoE under contract no. W-7405-ENG-48.

References

- [1] In the World Wide Web at <http://Physics.nist.gov/PhysRefData/contents.html>
- [2] Bastin T, Biémont E, Dumont P-D, Garnir H-P, Krenzer M J and Bukow H 1997 *J. Opt. Soc. Am.* **14** 1319
- [3] Bastin T, Biémont E, Dumont P-D, Garnir H-P, Krenzer M J, Bukow H and Kramida A E 1997 *Phys. Scr.* **55** 654
- [4] Kramida A E, Bastin T, Biémont E, Dumont P-D and Garnir H-P 1999 *Eur. Phys. J. D* **7** 525
- [5] Kramida A E, Bastin T, Biémont E, Dumont P-D and Garnir H-P 1999 *Eur. Phys. J. D* **7** 547
- [6] Kramida A E, Bastin T, Biémont E, Dumont P-D and Garnir H-P 1999 *J. Opt. Soc. Am.* **16** 1966
- [7] Träbert E, Doerfert J, Granzow J, Büttner R, Staude U, Schartner K-H, Rymuza P, Mokler P H, Engström L and Hutton R 1994 *Phys. Lett. A* **188** 355

- [8] Träbert E, Doerfert J, Granzow J, Büttner R, Staude U, Schartner K-H, Rymuza P, Engström L and Hutton R 1995 *Z. Phys. D* **32** 295
- [9] Träbert E, Staude U, Bosselmann P, Schartner K-H, Mokler P H and Tordoir X 1998 *Eur. Phys. J. D* **2** 117
- [10] Träbert E, Beiersdorfer P, Lepson J K and Chen H 2003 *Phys. Rev. A* **68** 042501
- [11] Dietrich D D, Chandler G A, Fortner R J, Hailey C J and Stewart R E 1985 *Phys. Rev. Lett.* **54** 1008
- [12] Beiersdorfer P *et al* 1988 *Phys. Rev. A* **37** 4153
- [13] Aglitskii E V, Ivanova E P, Panin S A, Safronova U I, Ulityn S I, Vainshtein L A and Wyart J-F 1989 *Phys. Scr.* **40** 601
- [14] Churilov S S, Joshi Y N, Reader J and Kildiyarova R R 2004 *Phys. Scr.* **70** 126
- [15] Tanuma H, Ohashi H, Shibuya E, Kobayashi N, Okuno T, Fujioka S, Nishimura H and Nishihara K 2005 *Nucl. Instrum. Methods B* **235** 331
- [16] Biedermann C, Radtke R, Fußmann G, Schwob J L and Mandelbaum P 2005 *Nucl. Instrum. Methods B* **235** 126
- [17] Kim Y-K, Baik D H, Indelicato P and Desclaux J P 1991 *Phys. Rev. A* **44** 148
- [18] Johnson W R, Blundell S A and Sapirstein J 1988 *Phys. Rev. A* **38** 2699
- [19] Safronova U I, Johnson W R and Berry H G 2000 *Phys. Rev. A* **61** 052503
- [20] Safronova U I, Namba C, Albritton J R, Johnson W R and Safronova M S 2002 *Phys. Rev. A* **65** 022507
- [21] Vilkas M J and Ishikawa Y 2005 *Phys. Rev. A* **72** 032512
- [22] Vilkas M J and Ishikawa Y 2004 *J. Phys. B: At. Mol. Opt. Phys.* **37** 1803
- [23] Sucher J 1980 *Phys. Rev. A* **22** 348
- [24] Mittleman M H 1981 *Phys. Rev. A* **24** 1167
- [25] Vilkas M J, Ishikawa Y and Koc K 1998 *Phys. Rev. E* **58** 5096
- [26] Savukov I M and Johnson W R 2002 *Phys. Rev. A* **65** 042053
- [27] Möller C and Plesset M S 1934 *Phys. Rev.* **46** 618
- [28] Vilkas M J and Ishikawa Y 2003 *Phys. Rev. A* **68** 012503
- [29] Vilkas M J and Ishikawa Y 2004 *Phys. Rev. A* **69** 062503
- [30] Ishikawa Y, Quiney H M and Malli G L 1991 *Phys. Rev. A* **43** 3270
- [31] Indelicato P, Gorceix O and Desclaux J P 1987 *J. Phys. B: At. Mol. Phys.* **20** 651
- [32] Kim Y-K 1990 Atomic processes in plasmas *AIP Conf. Proc.* **206** 19
- [33] Mohr P J 1992 *Phys. Rev. A* **46** 4421
- [34] Büttner R, Kraus B, Schartner K-H, Folkmann F, Mokler P H and Möller G 1992 *Z. Phys. D* **22** 693
- [35] Staude U, Bosselmann Ph, Büttner R, Horn D, Schartner K-H, Folkmann F, Livingston A E, Ludziejewski Th and Mokler P H 1998 *Phys. Rev. A* **58** 3516
- [36] Bosselmann Ph, Staude U, Horn D, Schartner K-H, Folkmann F, Livingston A E and Mokler P H 1999 *Phys. Rev. A* **59** 1874
- [37] Feili D, Bosselmann P, Schartner K-H, Folkmann F, Livingston A E, Träbert E, Ma X and Mokler P H 2000 *Phys. Rev. A* **62** 022501
- [38] Feili D, Zimmermann B, Neacsu C, Bosselmann P, Schartner K-H, Folkmann F, Livingston A E, Träbert E and Mokler P H 2005 *Phys. Scr.* **71** 48
- [39] Livingston A E, Büttner R, Zacarias A S, Kraus B, Schartner K-H, Folkmann F and Mokler P H 1997 *J. Opt. Soc. Am.* **14** 522
- [40] Reader J, Kaufman V, Sugar J, Ekberg J O, Feldman U, Brown C M, Seely J F and Rowan W L 1987 *J. Opt. Soc. Am. B* **4** 1821
- [41] Ekberg J O, Feldman U, Seely J F and Brown C M 1989 *Phys. Scr.* **40** 643
- [42] Ekberg J O, Feldman U, Seely J F, Brown C M, MacGowan B J, Kania D R and Keane C J 1991 *Phys. Scr.* **43** 19
- [43] Shima K, Kuno N, Yamanouchi M and Tawara H 1992 *At. Data Nucl. Data Tables* **51** 173
- [44] Beiersdorfer P *et al* 1988 *Phys. Rev. A* **37** 4153
- [45] Safronova U I, Safronova M S and Bruch R 1994 *Phys. Scr.* **49** 446
- [46] Cogordan J A and Lunell S 1986 *Phys. Scr.* **33** 406
- [47] Ivanova E P and Gulov A V 1991 *At. Data Nucl. Data Tables* **49** 1
- [48] Seely J F and Wagner R A 1990 *Phys. Rev. A* **41** 5246
- [49] Theodosiou C E and Curtis L J 1988 *Phys. Rev. A* **38** 4435
- [50] Blundell S A 1993 *Phys. Rev. A* **47** 1790
- [51] Cheng K T and Johnson W R 1977 *Phys. Rev. A* **16** 263
- [52] Ivanov L N and Ivanova E P 1979 *At. Data Nucl. Data Tables* **24** 95
- [53] Curtis L J and Ramanujam P S 1983 *J. Opt. Soc. Am.* **73** 979
- [54] Ivanova E P, Ivanov L N and Tsirekidze M A 1986 *At. Data Nucl. Data Tables* **35** 419
- [55] Curtis L J 1991 *Phys. Scr.* **43** 137

- [56] Marques J P, Parente F and Indelicato P 1993 *At. Data Nucl. Data Tables* **55** 157
- [57] Zou Y and Froese Fischer C 2001 *J. Phys. B: At. Mol. Opt. Phys.* **34** 915
- [58] Huang K-N 1986 *At. Data Nucl. Data Tables* **34** 1
- [59] Jupén C and Curtis L J 1996 *Phys. Scr.* **53** 312
- [60] Huang K-N 1985 *At. Data Nucl. Data Tables* **32** 503
- [61] Jupén C, Martinson I and Denne-Hinnov B 1991 *Phys. Scr.* **44** 562
- [62] Bengtsson P, Ando K, Kambara T, Awaya Y and Hutton R 1997 *Phys. Scr. T* **73** 81
- [63] Träbert E 1999 *Phys. Scr.* **59** 443
- [64] Ishikawa Y and Vilkas M J 2002 *Phys. Scr.* **65** 219
- [65] Huang M, Andersson M, Brage T, Hutton R, Jönsson P, Chongyang C and Zou Y 2005 *J. Phys. B: At. Mol. Opt. Phys.* **38** 503
- [66] Beiersdorfer P, Träbert E, Chen H, Chen M-H, May M J and Osterheld A L 2003 *Phys. Rev. A* **67** 052103
- [67] Bar-Shalom A, Klapisch M and Oreg J 1988 *Phys. Rev. A* **38** 1773
- [68] Bar-Shalom A, Klapisch M and Oreg J 2001 *J. Quantum Spectrosc. Radiat. Transfer* **71** 169
- [69] Gu M F 2003 *Astrophys. J.* **582** 1241
- [70] Froese Fischer C and Godefroid M 1982 *Nucl. Instrum. Methods B* **202** 307
- [71] Hutton R, Engström L and Träbert E 1988 *Nucl. Instrum. Methods B* **31** 294
- [72] Träbert E, Pinnington E H, Kernahan J A, Doerfert J, Granzow J, Heckmann P H and Hutton R 1996 *J. Phys. B: At. Mol. Phys.* **29** 2647
- [73] Träbert E, Calamai A G, Gwinner G, Knystautas E J, Pinnington E H and Wolf A 2003 *J. Phys. B: At. Mol. Opt. Phys.* **36** 1129
- [74] Träbert E 1998 *Mon. Not. R. Astron. Soc.* **297** 399
- [75] Träbert E 1981 *Phys. Scr.* **23** 253
- [76] Träbert E, Beiersdorfer P, Brown G V, Boyce K R, Kelley R L, Kilbourne C A, Porter F S and Szymkowiak A 2006 *Phys. Rev. A* **73** 022508
- [77] Safronova U I, Namba C, Murakami I, Johnson W R and Safronova M S 2001 *Phys. Rev. A* **64** 012507